

Molecular Orientation-Induced Second-Harmonic Generation: Deciphering Different Contributions Apart

Amit Beer, Ran Damari, Yun Chen, and Sharly Fleischer*



Cite This: *J. Phys. Chem. A* 2022, 126, 3732–3738



Read Online

ACCESS |



Metrics & More

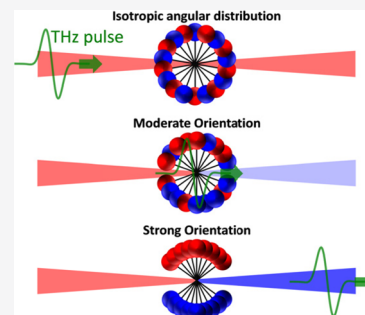


Article Recommendations



Supporting Information

ABSTRACT: We demonstrate and explore an all-optical technique for direct monitoring of the orientation dynamics in gas-phase molecular ensembles. The technique termed “MOISH” utilizes the transiently lifted inversion symmetry of polar gas media and provides a sensitive and spatially localized probing of the second-harmonic generation signal that is directly correlated with the orientation of the gas. Our experimental results reveal selective electronic and nuclear dynamical contributions to the overall nonlinear optical signal and decipher them apart using the “reporter gas” approach. “MOISH” provides new crucial means for implementing advanced coherent rotational control via concerted excitation by both terahertz and optical fields.



INTRODUCTION

Angular control of gas molecules is a long-standing goal of physics and chemistry, aimed to lift the inherent isotropy of gas molecules to aid the extraction of spectroscopic signatures from the molecular frame. Vast research efforts have successfully yielded a plethora of new observations and possibilities over the years, ranging from basic light-matter phenomena through novel spectroscopic methods for studying rotational dynamics to practical coherent control schemes and many more.^{1–6} Anisotropic angular distributions are categorized as “aligned” or “oriented”, referring to the preferable distribution of the *intramolecular axis* along a specific lab-frame axis or the *molecular dipoles* toward a specific lab-frame direction, respectively.^{7,8} Correspondingly, alignment retains the inversion symmetry of the medium, whereas orientation entails its inversion asymmetry upon orientation of the molecular dipoles toward the $+z$ or $-z$ direction (“up” or “down”).^{9,10} The lifted inversion symmetry provides access to nonlinear optical responses of even orders in the field ($\propto E^{2n}$) that are otherwise forbidden in unordered gas samples. Orientation may be induced by two-color laser field,^{11–14} mixed field (dc + optical pulse),^{15,16} or terahertz (THz) field excitations^{8,17–20} that interact resonantly via the permanent molecular dipole. Furthermore, intense THz fields have shown to induce molecular alignment in liquid and gas phases via the terahertz Kerr effect that is detected via time-resolved optical birefringence measurements.^{8,10,21–23} We note that non-resonant near-infrared (NIR) pulses with twisted polarizations have recently shown to induce molecular orientation.^{24,25}

THz fields induce molecular orientation by dipole interaction with polar molecules $\hat{V} = -\vec{\mu} \cdot \vec{E}$ to create a rotational wavepacket $\psi(t) = \sum c_{J,m} e^{-i\hat{H}t/\hbar} |J, m\rangle$, where

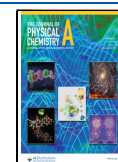
$\hat{H} = \frac{\hat{L}^2}{2I}$ with \hat{L} being the angular momentum operator, $|J, m\rangle$ the spherical harmonic functions, and their expansion coefficients $c_{J,m}$. The rotational wavepacket $\psi(t)$ periodically reproduces itself at integer multiples of the “rotational revival time”,^{26,27} given by $T_{\text{rev}} = \frac{1}{2B}$ (B is the rotational constant of the molecule).

As the gas molecules periodically orient, they form a transient macroscopic dipole that manifests by the emission of THz bursts, usually referred to as free-induction signals (FIDs)^{8,18,19,28} detectable via time-resolved electro-optic sampling (EOS).^{29,30} EOS provides an indirect signature of orientation because the radiated FID signals follow the time-derivative of the orientation $-d\langle \cos \theta \rangle / dt$ rather than the orientation $\langle \cos \theta \rangle$ itself.^{8,31} The main obstacle imposed by EOS (and FID) as a probe of molecular orientation emanates from the fact that the FID signals are accumulated throughout the entire interaction volume of the THz field and the gas, thereby lacking any spatial resolution. While the latter enables rotational spectroscopic measurements, it compromises and even practically impedes advanced coherent control schemes. For example, FID signals that emanate from nonlinear THz excitation at the focus of the THz field are accompanied and practically embedded in large FID signals irradiated from the entire volume, where the THz amplitude is much lower and

Received: May 10, 2022

Revised: May 15, 2022

Published: June 2, 2022



the signals are governed by the linear response to the field. The most relevant example for our research endeavors is the utilization of both NIR and THz fields in concert for advanced control of molecular dynamics. While an NIR pulse interacts with the molecules via the anisotropic polarizability tensor, THz fields interact through the permanent molecular dipoles, together providing two distinct rotational control handles.¹⁹ The extreme difference in volumetric foot-prints of the THz and NIR in the gas sample, with focal diameters of ~ 3 mm and ~ 50 μm , respectively, practically thwarts the detection of FID signals that selectively arise from molecules that experienced both the NIR and THz excitations. Motivated by the need for spatially localized detection of molecular orientation, we set to monitor the transient inversion asymmetry of the gas via the SHG ($\lambda_s = 400$ nm) of a NIR probe ($\lambda_{\text{probe}} = 800$ nm).

EXPERIMENTAL METHODS

The experimental approach presented hereafter is closely related to the THz field-induced SHG (TFISH)^{32–36} technique used for the detection of broad-band THz fields. TFISH relies on the nonlinear mixing of three input fields—a THz field (E_{THz}) and two NIR fields (E_{ω} , E_{ω}) via the third-order susceptibility, $\chi^{(3)}$, to yield a signal field at frequency $\omega_{\text{TFISH}} \cong 2\omega$. While TFISH is restricted to nonpolar gases³³ and typically performed in ambient air, “MOISH” aims to probe the rotational dynamics of polar gas samples that are resonantly excited by THz fields and manifest transient orientation dynamics long after the THz field is over. Special efforts are made to decipher the electronic (TFISH) and nuclear orientation (MOISH) contributions apart at the fundamental times of the rotational evolution of polar gases.

The experimental setup used in this work is similar to that reported in ref 35. Briefly, intense THz and NIR probe beams are routed to propagate collinearly and focus inside a static gas cell equipped with a designated <1 mm aperture. The latter effectively restricts the interaction length of the two beams and eases the phase-mismatch (Δk) of the generated SH signal. The NIR pulse (100 fs duration, 6 μJ pulse energy) is focused by a lens ($f = 150$ mm) such that its intensity remains well below the laser-induced plasma regime.^{35,37,38} Complementary EOS measurements were performed in our home-built time-domain THz spectrometer.^{18,19}

RESULTS AND DISCUSSION

Figure 1 compares the experimental results obtained with EOS and MOISH from methyl-iodide (CH_3I) gas (10 torr, 300 K) following irradiation by a single-cycle THz field generated by optical rectification in a LiNbO_3 crystal.³⁹ In EOS, the THz field propagates through the static gas cell located at the first focus of a 4-f setup.^{18,19} The THz (and succeeding FID) are recollimated and focused onto the EO detection crystal (GaP) and sampled by a weak NIR probe. Figure 1a,b shows the EOS signal with the input THz field (Figure 1a, at $t = 0$) and the FID emission at the first revival of the gas (Figure 1b, $T_{\text{rev}} \sim 66$ ps).^{31,40–42} Figure 1c,d depicts the time-resolved MOISH signal at the same respective intervals. Here, the THz field and the NIR pulse copropagate to focus at the center of the static gas cell and the generated SH signal is recorded as a function of their delay apart. While EOS detects the THz radiation (FID), MOISH is primarily sensitive to the degree of molecular orientation $\langle \cos \theta \rangle$. This is evident from the difference in signals' amplitudes of the incident THz field ($t =$

0) and the FID emission at the revival time; In EOS, the incident THz field reaches a peak value of 0.5 while the FID emitted at $t = T_{\text{rev}}$ remains well below 0.1 (in the arb. units shared by Figure 1a,b).

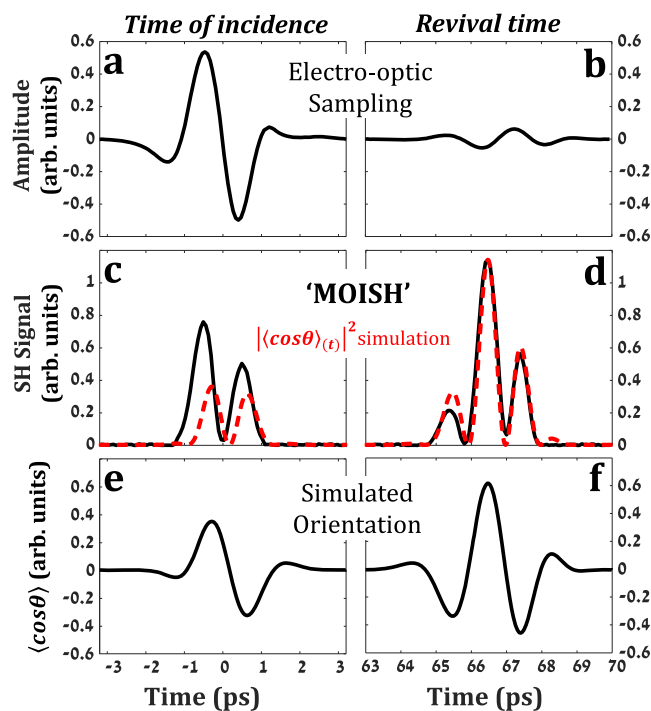


Figure 1. THz-induced orientation of 10 torr methyl-iodide (CH_3I) at room temperature. (a) and (b) EOS signal at $t = 0$ and at $t = 1T_{\text{rev}}$ respectively. (c) and (d) Second-harmonic (MOISH) signal (probe intensity 1.1×10^{14} W/cm^2) at $t = 0$ and at $t = 1T_{\text{rev}}$ respectively. (e) and (f) Simulated orientation dynamics at $t = 0$ and at $t = 1T_{\text{rev}}$ respectively.

In contrast, the MOISH signal obtained at $T_{\text{rev}} \sim 66$ ps (Figure 1d) is $\sim 50\%$ larger than that of the incident THz field (Figure 1c), in good agreement with the simulated orientation dynamics $\langle \cos \theta \rangle_{(t)}$ (Figure 1e,f). Note that the dashed red line in Figure 1c,d shows the absolute value squared $|\langle \cos \theta \rangle_{(t)}|^2$ of the simulation results shown in Figure 1e,f because MOISH provides a homodyne signal. The maximal orientation signal at $t = T_{\text{rev}}$ and not during, or in the vicinity of the THz excitation is an intriguing signature for the resonant nature of the THz-dipole interaction, indicating that the molecules continue to accumulate rotational energy in a coherent manner throughout the entire interaction with the field and beyond the initial event of orientation around $t = 0$. These rotational coherences manifest later on by enhanced orientation at $t = T_{\text{rev}}$, long after the THz field is over.^{8,17} We note that while CH_3I is a symmetric top, with rotational constants ($B = C = 0.25$ cm^{-1} , $A = 5.17$ cm^{-1}), the rotational dynamics responses of the methyl group are hindered in both THz orientation and NIR alignment experiments. In fact, previous studies have shown that the rotational dynamics of CH_3I is fully captured when modeled as a linear rotor with $B = 0.25$ cm^{-1} .^{31,41}

While the MOISH signals in Figure 1c,d are qualitatively in agreement with the theoretical predictions of Figure 1e,f (dashed red lines), in what follows we focus on their quantitative discrepancies. The main disagreement is revealed when comparing the ratio of the $t = T_{\text{rev}}$ signal ($S_{T_{\text{rev}}}$) and the $t =$

= 0 signal (S_0) given by $R_{\text{MOISH}} = \int S_{T_{\text{rev}}} dt / \int S_0 dt$ to the simulated ratio $R_{\text{Orient}}^{\text{theory}} = \int |\langle \cos \theta \rangle_{(T_{\text{rev}})}|^2 dt / \int |\langle \cos \theta \rangle_{(0)}|^2 dt$. The latter was found to be $R_{\text{Orient}}^{\text{theory}} \sim 2.8$ and insensitive to the carrier-envelope phase (CEP, see Supporting Information SI.1, which includes refs 43, 44.) of the THz field, whereas the experimental R_{MOISH} in Figure 1c,d yields $R_{\text{MOISH}} = 1.8$. The discrepancy in Figure 1c of the relative peak intensities and the slight temporal shift between the experimental (black curve) and simulated results (dashed red curve) is readily observed and will become clearer in what follows.

In a set of measurements performed with different polar gas species at varying pressures, we have found that R_{MOISH} varies with both the type and density of the gas, as shown in Figure 2

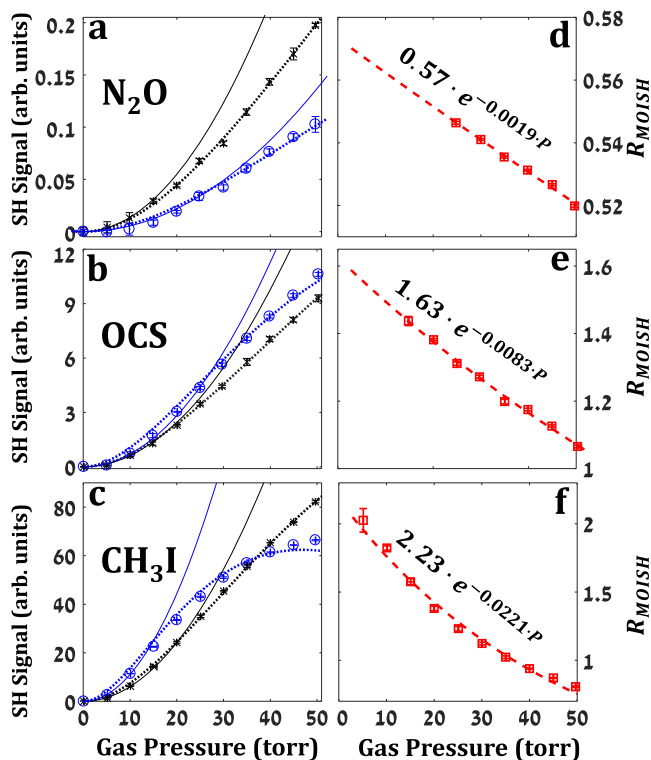


Figure 2. Experimental MOISH signals from different gases at varying pressures. (a–c) Show the integrated signals at $t = 0$ (black x 's and dotted trend-line) and at $t = 1T_{\text{rev}}$ (blue circles and dotted trend-line) from N_2O , OCS , and CH_3I respectively. (d–f) Show the R_{MOISH} of the signals in (a–c), respectively. All measurements were performed with a probe intensity of $\sim 3 \times 10^{13} \text{ W/cm}^2$. The expected quadratic pressure dependence is depicted by the solid black and blue lines, respectively.

for three different gas species (CH_3I , OCS , and N_2O) in the pressure range of 0–50 torr. We note that Figures 2a–c and 4a share the same intensity scale (given in arb. units) demonstrating that the CH_3I signal is 1–2 orders of magnitude larger than those of OCS and N_2O . This large variation emanates from the first-order (β) and second-order (γ) hyperpolarizabilities of the different gases as predicted by our calculations (for computational details see Supporting Information SI.3 that includes refs 45–62).

Figure 2a–c depict the SHG measured at $t = 0$ ($\int S_0 dt$, black data points) and $t = T_{\text{rev}}$ ($\int S_{T_{\text{rev}}} dt$, blue data points) for the three gas samples. The solid black and blue lines show the expected SHG dependence on pressure, produced by

extrapolation of the quadratic fit of the first few (low pressure) data points. Trend-lines of the experimental data sets are given by the dotted curves. The deviation of the experimental SH from quadratic pressure dependence is attributed to:

- (1) Collisional decoherence that effectively attenuates $S_{T_{\text{rev}}}$ and hardly affects S_0 .
- (2) Phase-mismatch experienced by the nonlinear SHG upon propagation in the gas.

Naturally, both these effects increase with gas density.

To ease the phase matching constraints, we restricted the interaction length by placing an iris in the gas cell.³⁵ Furthermore, we note that the SHG signals at $t = 0$ and $t = T_{\text{rev}}$ are affected similarly by phase-mismatch, thus their ratio (R_{MOISH}) is insensitive to phase-mismatch ramifications. Figure 2d–f depict the R_{MOISH} obtained from the data in 2a–c, respectively. Owing to the collisional decoherence, R_{MOISH} decays exponentially with pressure at a specific rate for each gas and is in good agreement with the decay rates obtained via EOS (see Supporting Information SI.2) and reported in ref 18. From the fitted exponential curves in Figure 2d–f, we find that the collision-free R_{MOISH} values (at $P = 0$, given by the pre-exponential factors) and $R_{\text{Orient}}^{\text{theory}} \sim 2.8$ remain in discrepancy ($R_{\text{MOISH}} = 0.57, 1.63, 2.23$ for N_2O , OCS , and CH_3I , respectively). This is attributed to the TFISH signal that is induced by the incident THz field ($t = 0$) and constructively adds to the MOISH signal. The sum of these two contributions increases S_0 (at the denominator of R_{MOISH}) and results in lower R_{MOISH} than that expected by orientation only. In what follows, we analyze the nuclear (MOISH) and electronic (TFISH) contributions to the nonlinear susceptibility of the medium, $\chi^{(2)}$, that give rise to the observed SHG signals.

A THz field induces instantaneous inversion asymmetry as it acts on the electronic cloud of the gas molecules, forcing the electrons to oscillate in the direction of the field. This results in an effective $\chi_{\text{elect}}^{(2)}$ that is detected via TFISH.³⁸ Although typically performed in air or other nonpolar gas samples, the THz-induced $\chi_{\text{elect}}^{(2)}$ is valid in polar molecules as well. In polar molecules however, the single-cycle THz field induces another type of inversion asymmetry as it orients the molecular dipoles^{7,8} and yields an effective $\chi_{\text{orient}}^{(2)}$ that enables MOISH.

Figure 3 depicts the distinct electronic and nuclear contributions at $t = 0$ and $t = T_{\text{rev}}$. The solid green curve in Figure 3a depicts the incident single-cycle THz field with an antisymmetric CEP, given by: $E_{\text{THz}}(t) = \exp\left(-\frac{t^2}{\sigma^2}\right) \cdot \cos(\omega_0 t + \pi/2)$, where $\sigma = \frac{1.5\text{ps}}{2\sqrt{\ln(2)}}$ and $\omega_0 = 0.5 \text{ THz}$. The electronic contribution induced by the field is instantaneous with the latter and depicted by the dashed blue curve in Figure 3a. The solid red curve depicts the nuclear contribution $\chi_{\text{orient}}^{(2)}$ of the oriented gas molecules $\langle \cos \theta \rangle_{(t)}$. The latter was simulated by numerically propagating the density matrix, ρ , via the Liouville–Von Neumann equation $\frac{\partial \rho}{\partial t} = -\frac{i}{\hbar} [\hat{H}, \rho]$, with $\hat{H} = \frac{\hat{p}^2}{2I} + \hat{V}$ and $\hat{V} = -\vec{\mu} \cdot \vec{E}_{\text{THz}}(t)$ the dipole interaction term.⁸ As can be seen in Figure 3a, the electronic and nuclear $\chi^{(2)}$ contributions induced by the incident THz field partially overlap. We note that the incident THz field and electronic response are normalized in Figure 3a. The orientation response (solid red) is normalized by its peak at $t = T_{\text{rev}}$ (Figure 3b, solid red curve). Another electronic contribution that may interfere with the orientation at $t = T_{\text{rev}}$ may be induced by the

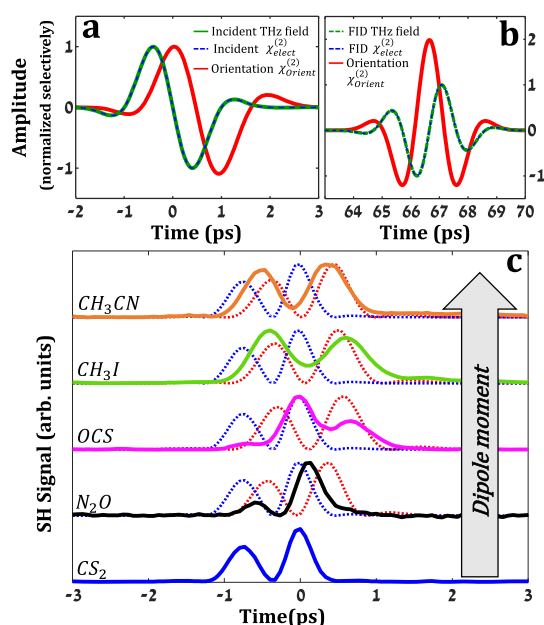


Figure 3. Simulation of the different $\chi^{(2)}$ contributions at (a) $t = 0$ and (b) $t = T_{\text{rev}}$. The green curve depicts the incident THz field resulting in electronic (dashed blue curve) and the nuclear orientation (solid red curve) contributions to the nonlinear susceptibility $\chi^{(2)}$. (c) Time-resolved SHG signal at the incidence of the THz field for different gases. The electronic and nuclear contributions to $\chi^{(2)}$ are depicted by the dotted blue and red curves, respectively.

emitted FID field (dashed blue curve in Figure 3b). The latter is given by the time derivative of the transient orientation^{29,30} (dashed green curve in Figure 3b).

To calculate R_{MOISH} , one needs to sum the $\chi_{\text{orient}}^{(2)}$ and $\chi_{\text{elect}}^{(2)}$ to obtain an effective $\chi^{(2)}$ for $t = 0$ and $t = T_{\text{rev}}$ selectively, with $\chi_{\text{elect}}^{(2)} \propto E_{\text{THz}} \gamma$ and $\chi_{\text{orient}}^{(2)} \propto E_{\text{THz}} \beta$, μ . Here, β and γ are the electronic hyper-polarizabilities at the probe frequency upon orientation and under the action of the THz field, respectively, and μ is the permanent dipole moment of the molecule. The obtained signals (in absolute value squared) are integrated over time and their ratio corresponds to R_{MOISH} . Because the amplitude of the emitted FID is $\sim 10^2$ fold smaller than that of the incident field (namely, $E_{\text{THz}}(0) \gg E_{\text{THz}}^{\text{FID}}(T_{\text{rev}})$ and thus $\chi_{\text{elect}}^{(2)}(0) \gg \chi_{\text{elect}}^{(2)}(T_{\text{rev}})$, the electronic contributions primarily increase the $t = 0$ signal and diminish the R_{MOISH} values as shown in Figure 2. The interplay between the two contributions at $t = 0$ is further manifested in the time-resolved signals of Figure 3c. Here, we extracted the incident E_{THz} from the pure electronic response of the (nonpolar) CS_2 gas. The same E_{THz} was used to simulate the transient orientation ($\langle \cos \theta \rangle_{(t)}$) for each gas selectively (dotted red lines in each panel). The pure electronic contribution (normalized) is plotted by the dotted blue line for reference. Figure 3c shows that while the temporal signal shapes of N_2O and OCS are admixtures of both the $\chi_{\text{elect}}^{(2)}$ and $\chi_{\text{orient}}^{(2)}$, the shapes of CH_3I and CH_3CN are primarily governed by the $\chi_{\text{orient}}^{(2)}$. The contribution of the latter becomes more profound with the increase in molecular dipole $\text{N}_2\text{O} \rightarrow \text{OCS} \rightarrow \text{CH}_3\text{I} \rightarrow \text{CH}_3\text{CN}$ (with $\mu = 0.17\text{D}, 0.72\text{D}, 1.62\text{D}, 3.92\text{D}$, respectively).

In what follows, we set to experimentally unveil the FID-induced $\chi_{\text{elect}}^{(2)}$ at $t = T_{\text{rev}}$. We start by considering the pressure-dependence of the different contributions discussed above: At $t = 0$, both the nuclear and electronic contributions are linear

with the number of molecules in the interaction region: $\chi_{\text{orient}}^{(2)}(0), \chi_{\text{elect}}^{(2)}(0) \propto P$. At $t = T_{\text{rev}}$, however, the two contributions differ in their pressure dependencies: while $\chi_{\text{orient}}^{(2)}(T_{\text{rev}}) \propto P$, the FID contribution depends on the density squared $\chi_{\text{elect}}^{(2)}(T_{\text{rev}}) \propto P^2$ because it is induced by the emitted FID ($\propto P$) that acts back on the same gas. Furthermore, when comparing different gases, one must consider their different dipole magnitudes. Consider a THz field E_{THz} interacting through the molecular dipole, $\mu \cdot E_{\text{THz}}$. Since the induced orientation $\langle \cos \theta \rangle$ is linear with μ , the FID that is emitted at $t = T_{\text{rev}}$ is quadratic with μ because $E_{\text{FID}} \propto -\frac{d\langle \cos \theta \rangle}{dt} \cdot \mu \cdot P^{18,63}$ where $\langle \cos \theta \rangle \propto \mu$ (for experimental E_{FID} vs μ see Supporting Information SI.4). From all of the above, we conclude that the extent to which the FID-induced $\chi_{\text{elect}}^{(2)}$ affects the MOISH signal at $t = T_{\text{rev}}$ depends on multiple factors: it increases with the hyperpolarizability (γ), the gas pressure ($\propto P^2$), and the molecular dipole ($\propto \mu^2$).

Thus, for gases with relatively low dipoles such as N_2O ($\mu = 0.17\text{D}$) and OCS ($\mu = 0.72\text{D}$) the contribution of the FID is negligible and the decay rate of the signal at $t = T_{\text{rev}}$ is effectively governed by collisions as shown in Figure 2a,b. For larger dipole values (such as CH_3I with $\mu = 1.62\text{D}$), we expect to find a larger decay rate than that induced solely from collisions. The decay rate of R_{MOISH} in Figure 2c however remains in good agreement with that quantified by EOS. This is attributed to the inherently large collisional decay of CH_3I that obscures the (relatively small) contribution of the FID at $t = T_{\text{rev}}$. Thus, a large molecular dipole acts as a “double-edged sword”—on the one hand, it increases the FID contribution but on the other hand—it enhances the collisional decay rate via dipole–dipole interactions that obscure the FID contribution. Nevertheless, an experimental indication for this elusive effect is presented in Figure 4a,b, where we conducted the exact same experiment of Figure 2 only for CH_3CN ($\mu = 3.92\text{D}$) and found that R_{MOISH} decays $\sim 30\%$ faster than that quantified by EOS.

To experimentally validate the above hypothesis, one would like to vary the relative magnitudes of the two $\chi^{(2)}$ contributions selectively; however those are unavoidably inter-related. Instead, we utilized a nonpolar gas that does not contribute to $\chi_{\text{orient}}^{(2)}$ but is strongly affected by the FID of the polar gas and hence serves as a “reporter gas”. This is done by injecting carbon-disulfide (CS_2) at varying partial densities in addition to the fixed density of the polar gas (CH_3I and CH_3CN in Figure 4c,d, respectively). For the gas-mixing procedure, see Supporting Information SI.5 which includes ref 64.

Curves shown in Figure 4c,d were obtained with a fixed partial pressure of 10 torr CH_3I , and 12 torr CH_3CN , respectively, and varying CS_2 pressures. The black curves show the expected $t = T_{\text{rev}}$ signal of the mixture with collisional decay and phase matching effects accounted for (see Supporting Information SI.6), but without the FID contribution. The blue data points (marked by “+”) and dashed trend-lines depict the experimental results. In both gas mixtures, the FID emission interacts with the reporter CS_2 gas and induces $\chi_{\text{elect}}^{(2)}$ that partially counteracts the $\chi_{\text{orient}}^{(2)}$ of the polar gas at $t = T_{\text{rev}}$, expediting the decay of the SH signal with increased CS_2 pressure. As the CS_2 pressure is further increased, the decay rate of the SH gradually reduces and its trend is reversed as the orientation- and FID-induced contributions become comparable (~ 30 torr in Figure 4d). Above this pressure, the SH signal

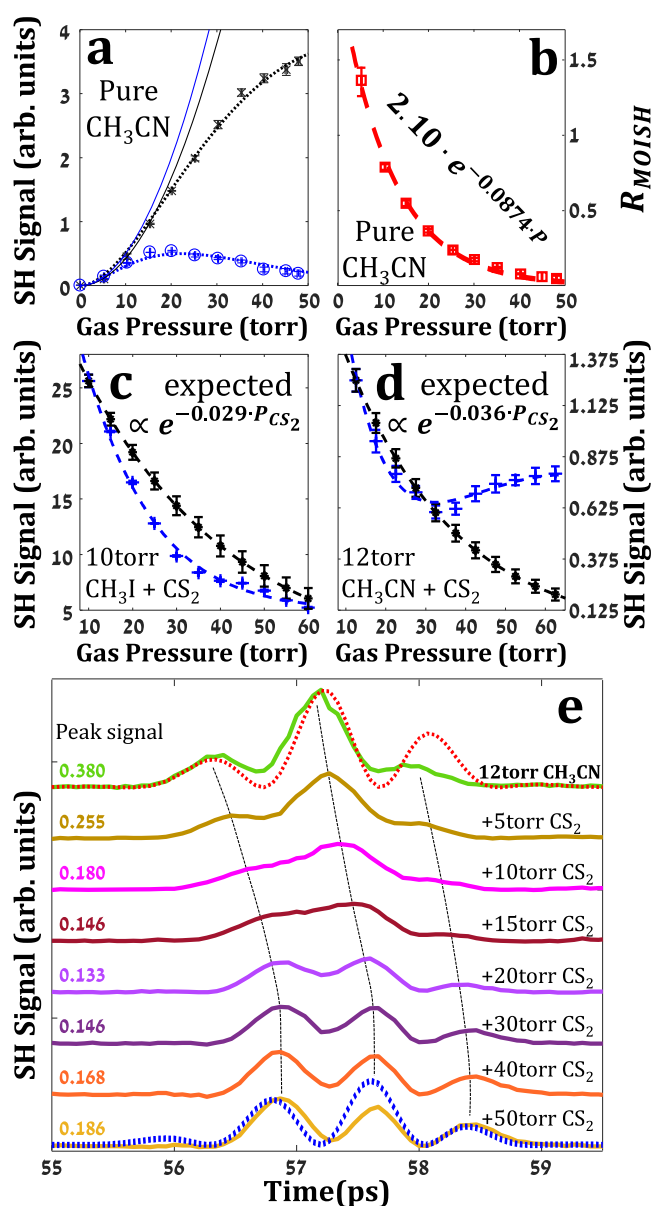


Figure 4. (a) and (b) Same as in Figure 2 only for CH_3CN . (c) SH signals from a mixture of 10 torr CH_3I and varying CS_2 pressure. Calculated decay shown in black, and experimental decay shown in blue. (d) Same as (c) for 12 torr CH_3CN and varying CS_2 pressure. (e) Time-resolved signals of the data of (d) showing the evolution of the signal shape from that of MOISH (solid green) to that of FID-induced TFISH (solid yellow). Corresponding simulated results are shown by the dotted red and blue transients, respectively. The peak signal amplitudes of each transient as marked in the figure.

starts to increase as the FID contribution overcomes that of the MOISH. This is shown in Figure 4e where the temporal shape of the signal gradually evolves from that of MOISH (from pure CH_3CN depicted by the solid green curve) to that of the FID-induced TFISH (solid yellow), in agreement with the simulated transients (dotted red and blue, respectively). In addition, the use of the reporter, nonpolar gas, provides yet another advantage over a pure polar gas sample as the decay of R_{MOISH} is significantly lower in the mixtures: with 4×10^{-3} and $6 \times 10^{-3} \text{ torr}^{-1}$ for the $\text{CH}_3\text{I}/\text{CS}_2$ and $\text{CH}_3\text{CN}/\text{CS}_2$ mixtures compared to 2.2×10^{-2} and $8.7 \times 10^{-2} \text{ torr}^{-1}$ in neat gases, respectively. The reduced decay rate improves the visibility of

the FID contribution that is otherwise obscured by the rapid decay rate of the pure polar gas. We further note that to alleviate possible contributions of THz-induced rotational excitation of CS_2 owing to its large polarizability anisotropy,^{21,22} we repeated the reporter gas experiment with carbon-tetrachloride (CCl_4) and obtained very similar trends as in Figure 4c,d.

CONCLUSIONS

To conclude, we utilized the SH signal generated in THz-oriented gas phase molecules as a direct probe of orientation. The technique coined “MOISH” is contributed by several electronic and nuclear (orientation) responses that temporally interfere and dictate the observed SH signal. These contributions were theoretically and experimentally explored in different gases and varying gas densities. A “reporter gas” approach was used to unveil the elusive contribution of the secondary FID emission. MOISH offers a spatially localized, all-optical technique for direct probing of molecular orientation and provides new means for studying coherent rotational dynamics induced by concerted THz and optical excitations.

ASSOCIATED CONTENT

Supporting Information

The Supporting Information is available free of charge at <https://pubs.acs.org/doi/10.1021/acs.jpca.2c03237>.

SI.1. Theoretical dependence of R_{orient} on the carrier envelope phase of the THz field, SI.2. Experimental collisional decay rates, SI.3. Theoretical calculations of the Hyperpolarizabilities, SI.4. FID dependence on the molecular dipole, SI.5. Gas mixing procedure, and SI.6. Phase-mismatch and collisional decay of MOISH in gas mixtures (PDF)

AUTHOR INFORMATION

Corresponding Author

Sharly Fleischer – Raymond and Beverly Sackler Faculty of Exact Sciences, School of Chemistry, Tel Aviv University, Tel Aviv 6997801, Israel; Tel-Aviv University Center for Light-Matter-Interaction, Tel Aviv 6997801, Israel; orcid.org/0000-0003-0213-2165; Email: sharlyf@tauex.tau.ac.il

Authors

Amit Beer – Raymond and Beverly Sackler Faculty of Exact Sciences, School of Chemistry, Tel Aviv University, Tel Aviv 6997801, Israel; Tel-Aviv University Center for Light-Matter-Interaction, Tel Aviv 6997801, Israel

Ran Damari – Raymond and Beverly Sackler Faculty of Exact Sciences, School of Chemistry, Tel Aviv University, Tel Aviv 6997801, Israel; Tel-Aviv University Center for Light-Matter-Interaction, Tel Aviv 6997801, Israel

Yun Chen – Raymond and Beverly Sackler Faculty of Exact Sciences, School of Chemistry, Tel Aviv University, Tel Aviv 6997801, Israel

Complete contact information is available at: <https://pubs.acs.org/doi/10.1021/acs.jpca.2c03237>

Notes

The authors declare no competing financial interest.

ACKNOWLEDGMENTS

The authors thank Prof. Oded Hod and Prof. Michael Urbakh (TAU chemistry) for stimulating discussions. SF acknowledges the support of Israel Science Foundation (926/18) and the Wolfson Foundation (PR/ec/20419).

REFERENCES

- (1) Fleischer, S.; Khodorkovsky, Y.; Gershnel, E.; Prior, Y.; Averbukh, I. S. Molecular Alignment Induced by Ultrashort Laser Pulses and Its Impact on Molecular Motion. *Isr. J. Chem.* **2012**, *52*, 414–437.
- (2) Stapelfeldt, H.; Seideman, T. Colloquium : Aligning Molecules with Strong Laser Pulses. *Rev. Mod. Phys.* **2003**, *75*, 543–557.
- (3) Lemesko, M.; Krems, R. V.; Doyle, J. M.; Kais, S. Manipulation of Molecules with Electromagnetic Fields. *Mol. Phys.* **2013**, *111*, 1648–1682.
- (4) Ohshima, Y.; Hasegawa, H. Coherent Rotational Excitation by Intense Nonresonant Laser Fields. *Int. Rev. Phys. Chem.* **2010**, *29*, 619–663.
- (5) Koch, C. P.; Lemesko, M.; Sugny, D. Quantum Control of Molecular Rotation. *Rev. Mod. Phys.* **2019**, *91*, No. 035005.
- (6) Lin, K.; Tutunnikov, I.; Ma, J.; Qiang, J.; Zhou, L.; Faucher, O.; Prior, Y.; Averbukh, I. S.; Wu, J. Spatiotemporal Rotational Dynamics of Laser-Driven Molecules. *Adv. Photon.* **2020**, *2*, 1.
- (7) Machholm, M.; Henriksen, N. E. Field-Free Orientation of Molecules. *Phys. Rev. Lett.* **2001**, *87*, No. 193001.
- (8) Fleischer, S.; Zhou, Y.; Field, R. W.; Nelson, K. A. Molecular Orientation and Alignment by Intense Single-Cycle THz Pulses. *Phys. Rev. Lett.* **2011**, *107*, No. 163603.
- (9) Lu, J.; Zhang, Y.; Hwang, H. Y. H. Y.; Ofori-Okai, B. K. B. K.; Fleischer, S.; Nelson, K. A. Nonlinear Two-Dimensional Terahertz Photon Echo and Rotational Spectroscopy in the Gas Phase. *Proc. Natl. Acad. Sci. U. S. A.* **2016**, *113*, 11800–11805.
- (10) Fleischer, S.; Field, R. W.; Nelson, K. A. Commensurate Two-Quantum Coherences Induced by Time-Delayed THz Fields. *Phys. Rev. Lett.* **2012**, *109*, No. 123603.
- (11) Frumker, E.; Hebeisen, C. T.; Kajumba, N.; Bertrand, J. B.; Wörner, H. J.; Spanner, M.; Villeneuve, D. M.; Naumov, A.; Corkum, P. B. Oriented Rotational Wave-Packet Dynamics Studies via High Harmonic Generation. *Phys. Rev. Lett.* **2012**, *109*, No. 113901.
- (12) de, S.; Znakovskaya, I.; Ray, D.; Anis, F.; Johnson, N. G.; Bocharova, I. A.; Magrakvelidze, M.; Esry, B. D.; Cocke, C. L.; Litvinyuk, I. V.; Kling, M. F. Field-Free Orientation of CO Molecules by Femtosecond Two-Color Laser Fields. *Phys. Rev. Lett.* **2009**, *103*, No. 153002.
- (13) Kraus, P. M.; Rupenyan, A.; Wörner, H. J. High-Harmonic Spectroscopy of Oriented OCS Molecules: Emission of Even and Odd Harmonics. *Phys. Rev. Lett.* **2012**, *109*, No. 233903.
- (14) Lin, K.; Tutunnikov, I.; Qiang, J.; Ma, J.; Song, Q.; Ji, Q.; Zhang, W.; Li, H.; Sun, F.; Gong, X.; Li, H.; Lu, P.; Zeng, H.; Prior, Y.; Averbukh, I. S.; Wu, J. All-Optical Field-Free Three-Dimensional Orientation of Asymmetric-Top Molecules. *Nat. Commun.* **2018**, *9*, 5134.
- (15) Hansen, J. L.; Omiste, J. J.; Nielsen, J. H.; Pentlehner, D.; Küpper, J.; González-Férez, R.; Stapelfeldt, H. Mixed-Field Orientation of Molecules without Rotational Symmetry. *J. Chem. Phys.* **2013**, *139*, 234313.
- (16) Nevo, I.; Holmegaard, L.; Nielsen, J. H.; Hansen, J. L.; Stapelfeldt, H.; Filsinger, F.; Meijer, G.; Küpper, J. Laser-Induced 3D Alignment and Orientation of Quantum State-Selected Molecules. *Phys. Chem. Chem. Phys.* **2009**, *11*, 9912.
- (17) Shu, C.-C.; Henriksen, N. E. Field-Free Molecular Orientation Induced by Single-Cycle THz Pulses: The Role of Resonance and Quantum Interference. *Phys. Rev. A* **2013**, *87*, No. 013408.
- (18) Damari, R.; Rosenberg, D.; Fleischer, S. Coherent Radiative Decay of Molecular Rotations: A Comparative Study of Terahertz-Oriented versus Optically Aligned Molecular Ensembles. *Phys. Rev. Lett.* **2017**, *119*, No. 033002.
- (19) Damari, R.; Kallush, S.; Fleischer, S. Rotational Control of Asymmetric Molecules: Dipole- versus Polarizability-Driven Rotational Dynamics. *Phys. Rev. Lett.* **2016**, *117*, No. 103001.
- (20) Babilotte, P.; Coudert, L. H.; Billard, F.; Hertz, E.; Faucher, O.; Lavorel, B. Experimental and Theoretical Study of Free Induction Decay of Water Molecules Induced by Terahertz Laser Pulses. *Phys. Rev. A* **2017**, *95*, No. 043408.
- (21) Hoffmann, M. C.; Brandt, N. C.; Hwang, H. Y.; Yeh, K.-L.; Nelson, K. A. Terahertz Kerr Effect. *Appl. Phys. Lett.* **2009**, *95*, 231105.
- (22) Hwang, H. Y.; Fleischer, S.; Brandt, N. C.; Perkins, B. G.; Liu, M.; Fan, K.; Sternbach, A.; Zhang, X.; Averitt, R. D.; Nelson, K. A. A Review of Non-Linear Terahertz Spectroscopy with Ultrashort Tabletop-Laser Pulses. *J. Mod. Opt.* **2015**, *62*, 1447–1479.
- (23) Shalaby, M.; Hauri, C. P. Air Nonlinear Dynamics Initiated by Ultra-Intense Lambda-Cubic Terahertz Pulses. *Appl. Phys. Lett.* **2015**, *106*, 181108.
- (24) Gershnel, E.; Averbukh, I. S. Orienting Asymmetric Molecules by Laser Fields with Twisted Polarization. *Phys. Rev. Lett.* **2018**, *120*, No. 083204.
- (25) Milner, A. A.; Fordyce, J. A. M.; Macphail-Bartley, I.; Wasserman, W.; Milner, V.; Tutunnikov, I.; Averbukh, I. S. Controlled Enantioselective Orientation of Chiral Molecules with an Optical Centrifuge. *Phys. Rev. Lett.* **2019**, *122*, No. 223201.
- (26) Felker, P. M.; Baskin, J. S.; Zewail, A. H. Rephasing of Collisionless Molecular Rotational Coherence in Large Molecules. *J. Phys. Chem.* **1986**, *90*, 124–728.
- (27) Averbukh, I. S.; Perelman, N. F. Fractional Revivals: Universality in the Long-Term Evolution of Quantum Wave Packets beyond the Correspondence Principle Dynamics. *Phys. Lett. A* **1989**, *139*, 449–453.
- (28) Harde, H.; Keiding, S.; Grischkowsky, D. THz Commensurate Echoes: Periodic Rephasing of Molecular Transitions in Free-Induction Decay. *Phys. Rev. Lett.* **1991**, *66*, 1834–1837.
- (29) Nahata, A.; Welington, A. S.; Heinz, T. F. A Wideband Coherent Terahertz Spectroscopy System Using Optical Rectification and Electro-Optic Sampling. *Appl. Phys. Lett.* **1996**, *69*, 2321.
- (30) Wu, Q.; Zhang, X.-C. Free-space Electro-optic Sampling of Terahertz Beams. *Appl. Phys. Lett.* **1995**, *67*, 3523–3525.
- (31) Babilotte, P.; Hamraoui, K.; Billard, F.; Hertz, E.; Lavorel, B.; Faucher, O.; Sugny, D. Observation of the Field-Free Orientation of a Symmetric-Top Molecule by Terahertz Laser Pulses at High Temperature. *Phys. Rev. A* **2016**, *94*, No. 043403.
- (32) Cook, D. J.; Chen, J. X.; Morlino, E. A.; Hochstrasser, R. M. Terahertz-Field-Induced Second-Harmonic Generation Measurements of Liquid Dynamics. *Chem. Phys. Lett.* **1999**, *309*, 221–228.
- (33) Chen, J.; Han, P.; Zhang, X.-C. Terahertz-Field-Induced Second-Harmonic Generation in a Beta Barium Borate Crystal and Its Application in Terahertz Detection. *Appl. Phys. Lett.* **2009**, *95*, No. 011118.
- (34) Karpowicz, N.; Lu, X.; Zhang, X.-C. Terahertz Gas Photonics. *J. Mod. Opt.* **2009**, *56*, 1137–1150.
- (35) Beer, A.; Hershkovitz, D.; Fleischer, S. Iris-Assisted Terahertz Field-Induced Second-Harmonic Generation in Air. *Opt. Lett.* **2019**, *44*, 5190.
- (36) Lu, X.; Karpowicz, N.; Zhang, X.-C. Broadband Terahertz Detection with Selected Gases. *J. Opt. Soc. Am. B* **2009**, *26*, A66.
- (37) Sunstov, S.; Abdollahpour, D.; Papazoglou, D. G.; Tzortzakakis, S. Filamentation-Induced Third-Harmonic Generation in Air via Plasma-Enhanced Third-Order Susceptibility. *Phys. Rev. A* **2010**, *81*, No. 033817.
- (38) Dai, J.; Xie, X.; Zhang, X.-C. Detection of Broadband Terahertz Waves with a Laser-Induced Plasma in Gases. *Phys. Rev. Lett.* **2006**, *97*, 103903.
- (39) Hebling, J.; Yeh, K.; Hoffmann, M. C.; Bartal, B.; Nelson, K. A. Generation of High-Power Terahertz Pulses by Tilted-Pulse-Front Excitation and Their Application Possibilities. *J. Opt. Soc. Am. B* **2008**, *25*, B6.

- (40) Rosenberg, D.; Damari, R.; Fleischer, S. Echo Spectroscopy in Multilevel Quantum-Mechanical Rotors. *Phys. Rev. Lett.* **2018**, *121*, No. 234101.
- (41) Rosenberg, D.; Damari, R.; Kallush, S.; Fleischer, S. Rotational Echoes: Rephasing of Centrifugal Distortion in Laser-Induced Molecular Alignment. *J. Phys. Chem. Lett.* **2017**, *8*, 5128–5135.
- (42) Hamilton, E.; Seideman, T.; Ejdrup, T.; Poulsen, M. D.; Bisgaard, C. Z.; Viftrup, S. S.; Stapelfeldt, H. Alignment of Symmetric Top Molecules by Short Laser Pulses. *Phys. Rev. A* **2005**, *72*, No. 043402.
- (43) Ahmed, S.; Savolainen, J.; Hamm, P. The Effect of the Gouy Phase in Optical-Pump-THz-Probe Spectroscopy. *Opt. Express* **2014**, *22*, 4256.
- (44) Owschimikow, N.; Königsmann, F.; Maurer, J.; Giese, P.; Ott, A.; Schmidt, B.; Schwentner, N. Cross Sections for Rotational Decoherence of Perturbed Nitrogen Measured via Decay of Laser-Induced Alignment. *J. Chem. Phys.* **2010**, *133*, No. 044311.
- (45) Becke, A. D. A New Mixing of Hartree–Fock and Local Density-functional Theories. *J. Chem. Phys.* **1993**, *98*, 1372–1377.
- (46) Krishnan, R.; Binkley, J. S.; Seeger, R.; Pople, J. A. Self-consistent Molecular Orbital Methods. XX. A Basis Set for Correlated Wave Functions. *J. Chem. Phys.* **1980**, *72*, 650–654.
- (47) Peterson, K. A.; Figgen, D.; Goll, E.; Stoll, H.; Dolg, M. Systematically Convergent Basis Sets with Relativistic Pseudopotentials. II. Small-Core Pseudopotentials and Correlation Consistent Basis Sets for the Post-d Group 16–18 Elements. *J. Chem. Phys.* **2003**, *119*, 11113–11123.
- (48) Weigend, F.; Ahlrichs, R. Balanced Basis Sets of Split Valence, Triple Zeta Valence and Quadruple Zeta Valence Quality for H to Rn: Design and Assessment of Accuracy. *Phys. Chem. Chem. Phys.* **2005**, *7*, 3297–3305.
- (49) Rappoport, D.; Furche, F. Property-Optimized Gaussian Basis Sets for Molecular Response Calculations. *J. Chem. Phys.* **2010**, *133*, No. 134105.
- (50) Weigend, F.; Furche, F.; Ahlrichs, R. Gaussian Basis Sets of Quadruple Zeta Valence Quality for Atoms H–Kr. *J. Chem. Phys.* **2003**, *119*, 12753–12762.
- (51) Hickey, A. L.; Rowley, C. N. Benchmarking Quantum Chemical Methods for the Calculation of Molecular Dipole Moments and Polarizabilities. *J. Phys. Chem. A* **2014**, *118*, 3678–3687.
- (52) Zalešny, R.; Baranowska-Ączkowska, A.; Medveř, M.; Luis, J. M. Comparison of Property-Oriented Basis Sets for the Computation of Electronic and Nuclear Relaxation Hyperpolarizabilities. *J. Chem. Theory Comput.* **2015**, *11*, 4119–4128.
- (53) Frisch, M. J.; Trucks, G. W.; Schlegel, H. B.; Scuseria, G. E.; Robb, M. A.; Cheeseman, J. R.; Scalmani, G.; Barone, V.; Petersson, G. A.; Nakatsuji, H.; Li, X. et al. *Gaussian 16, Revision C.01*; Gaussian, Inc.: Wallin, 2016, p. G16_C01.
- (54) Lu, T.; Chen, F. Multiwfn: A Multifunctional Wavefunction Analyzer. *J. Comput. Chem.* **2012**, *33*, 580–592.
- (55) Champagne, B.; Perpète, E. A.; Jacquemin, D.; Van Gisbergen, S. J. A.; Baerends, E. J.; Soubra-Ghaoui, C.; Robins, K. A.; Kirtman, B. Assessment of Conventional Density Functional Schemes for Computing the Dipole Moment and (Hyper)Polarizabilities of Push-Pull π -Conjugated Systems. *J. Phys. Chem. A* **2000**, *104*, 4755–4763.
- (56) Salek, P.; Helgaker, T.; Vahtras, O.; Ågren, H.; Jonsson, D.; Gauss, J. A Comparison of Density-Functional-Theory and Coupled-Cluster Frequency-Dependent Polarizabilities and Hyperpolarizabilities. *Mol. Phys.* **2005**, *103*, 439–450.
- (57) Autschbach, J.; Srebro, M. Delocalization Error and “Functional Tuning” in Kohn–Sham Calculations of Molecular Properties. *Acc. Chem. Res.* **2014**, *47*, 2592–2602.
- (58) Vydrov, O. A.; Scuseria, G. E.; Perdew, J. P.; Ruzsinszky, A.; Csonka, G. I. Scaling down the Perdew–Zunger Self-Interaction Correction in Many-Electron Regions. *J. Chem. Phys.* **2006**, *124*, No. 094108.
- (59) Adamo, C.; Barone, V. Toward Reliable Density Functional Methods without Adjustable Parameters: The PBE0 Model. *J. Chem. Phys.* **1999**, *110*, 6158–6170.
- (60) Dunning, T. H. Gaussian Basis Sets for Use in Correlated Molecular Calculations. I. The Atoms Boron through Neon and Hydrogen. *J. Chem. Phys.* **1989**, *90*, 1007–1023.
- (61) Kendall, R. A.; Dunning, T. H.; Harrison, R. J. Electron Affinities of the First-Row Atoms Revisited. Systematic Basis Sets and Wave Functions. *J. Chem. Phys.* **1992**, *96*, 6796–6806.
- (62) Woon, D. E.; Dunning, T. H. Gaussian Basis Sets for Use in Correlated Molecular Calculations. III. The Atoms Aluminum through Argon. *J. Chem. Phys.* **1993**, *98*, 1358–1371.
- (63) Fleischer, S.; Field, R. W.; Nelson, K. A. From Populations to Coherences and Back Again: A New Insight about Rotating Dipoles. *arXiv* **2014**, arXiv:1405.7025.
- (64) Wilson, R. R. A Vacuum-Tight Sliding Seal. *Rev. Sci. Instrum.* **1941**, *12*, 91–93.